

Butterfly Echo Protocol for Axis-Agnostic Heisenberg-Limited Metrology

Jacob Bringewatt,^{1,2,*} Leon Zaporski,^{3,*} Matthew Radzihovsky,³ Jasmine Albert,⁴ Alexey V. Gorshkov,^{5,6} Vladan Vuletić,³ and Gregory Bentsen⁴

¹*The Volgenau Department of Physics, United States Naval Academy, Annapolis, MD 21402, USA*

²*Department of Physics, Harvard University, Cambridge, MA 02138, USA*

³*MIT-Harvard Center for Ultracold Atoms and Research Laboratory of Electronics, Massachusetts Institute of Technology, Cambridge, Massachusetts 02139, USA*

⁴*Department of Physics, The College of William & Mary*

⁵*Joint Center for Quantum Information and Computer Science, NIST/University of Maryland, College Park, Maryland 20742, USA*

⁶*Joint Quantum Institute, NIST/University of Maryland, College Park, Maryland 20742, USA*

(Dated: February 27, 2026)

The extreme sensitivity of chaotic systems to external perturbations makes them natural candidates for sensing applications. We propose a single-shot echo-based protocol for estimating small rotations about an unknown axis that leverages random symmetric probe states prepared via chaotic dynamics. In contrast to previous protocols for this axis-agnostic rotation sensing problem that depend on difficult-to-prepare anticoherent states, the random probe states used in our protocol can be prepared via constant-depth chaotic circuits composed of random one-axis twisting pulses. We demonstrate analytically that our protocol achieves Heisenberg scaling relative to an arbitrary rotation axis that need not be a priori known. We also investigate the effects of collective and single-particle dephasing in our protocol using analytical and numerical tools. While the requirements on dephasing rates to maintain Heisenberg sensitivity are strict, they are achievable in near-term experiments, for instance, for magnetometric rotsensing with high-spin lanthanide atoms such as dysprosium-164.

Quantum metrology harnesses many-body entanglement to enable precision measurements beyond the capabilities of uncorrelated probes [1]. Whereas the measurement precision of N unentangled sensors is limited by the standard quantum limit (SQL) with sensitivity scaling as $\sim 1/\sqrt{N}$, entangled probe states can surpass this limit, allowing for Heisenberg-scaling sensitivity $\sim 1/N$. These theoretical limits are difficult to achieve in practice, however. Optimal probe states, such as the Greenberger–Horne–Zeilinger (GHZ) state, are extremely sensitive to external perturbations, motivating the development of alternative schemes that sacrifice some amount of optimality—either in sensitivity or in signal bandwidth—to gain some degree of robustness (although see Refs. [2, 3]). Examples include squeezed states [4–7], which are less vulnerable to particle loss than GHZ states, and echo-based protocols [8–15], which have intrinsic robustness to readout noise.

On the other hand, high sensitivity to external fields of interest lends itself naturally to sens-

ing applications. In particular, chaotic systems are extremely sensitive to external perturbations due to the so-called butterfly effect where small perturbations—such as a butterfly flapping its wings—are rapidly amplified into large changes in system behavior.

In this Letter, we leverage this high sensitivity to develop a single-shot echo sensing protocol based on quantum information scrambling for axis-agnostic rotation sensing. Random or chaotic dynamics have been previously considered as a metrological resource [16, 17], and echo-based protocols have also seen significant recent interest [8–15]. These two ideas have been previously combined to yield Heisenberg-limited sensing of rotations about a known axis in Ref. [17]. Our work demonstrates how chaos and echo-based protocols also provide a natural way to simultaneously enable optimal sensitivity scaling for a whole class of unknown signals (in this case rotations about an unknown axis). Thus, this randomization-driven robustness to different parameter encodings provides

another example of how scrambling can be used as a metrological resource.

Probes that are sensitive to different types of parameter encodings are of clear interest. The simplest examples of such probes are quantum sensors designed to estimate a rotation angle about an unknown axis even in the single-shot limit. Also known as quantum rotosensors [18, 19], they find diverse applications, ranging from entanglement-enhanced gyroscopes for inertial navigation [20] to tests of general relativity [21] to reference frame alignment [22]. For small angles, the optimal probe states for rotosensing [23, 24] are the so-called anticonherent states [20, 22, 25, 26]. However, with the GHZ state being the lowest-order anticonherent state, preparing highly anticonherent states for large N is a significant challenge [27].

Here, we propose an alternative *butterfly echo protocol* (Fig. 1) for estimating small rotations about an unknown axis that leverages random pure probe states from the symmetric subspace spanned by symmetric Dicke states, $\mathcal{S}_N := \text{span}\{|S, m\rangle\}$ where $-S \leq m \leq S$ and $S = N/2$ is the total spin. States in this space (which include the anticonherent states) are well-known to be useful resources for quantum metrology in a variety of contexts [28–30]. In the butterfly echo protocol, we use the fact that while a randomly chosen state from \mathcal{S}_N is not, in general, perfectly anticonherent, such states are anticonherent *on average*. We demonstrate that, properly defined, this averaged notion of anticonherence is sufficient to obtain Heisenberg scaling in the estimation of a small rotation angle with high probability.

While, up to a small constant, the signal-to-noise ratio for our protocol is optimal, the signal bandwidth, as with all echo-based protocols [31], is necessarily small. Consequently, while ensembles of random symmetric states are more robust and simpler to prepare than anticonherent states, noise remains a significant barrier to experimental realization of the protocol. Aiming at understanding these limitations we numerically analyze a random one-axis twisting (OAT) scheme for preparing the random probe states in the butterfly echo protocol and examine the effects of noise in this model. These results are supported via analytic calculations in the limit of

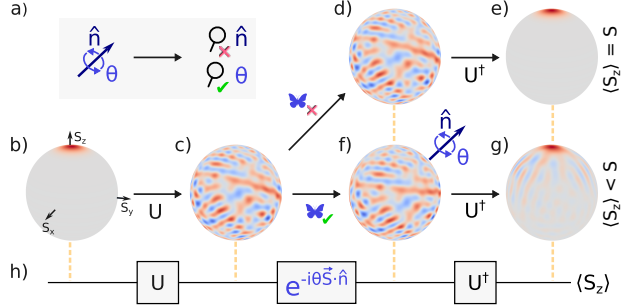


FIG. 1. **The butterfly echo protocol** reveals information about a rotation angle θ with Heisenberg-scaling without revealing information about an arbitrary, a priori unknown, rotation axis \hat{n} (a). An initially spin-polarized state (b) is scrambled by chaotic dynamics U into a random probe state (c). Absent a rotation (d) the probe state returns to its original spin-polarized state (e) under time reversal U^\dagger . By contrast, a nonzero rotation (f) leads to imperfect time-reversal and a commensurate reduction in spin polarization $\langle S_z \rangle$. Bloch spheres show representative Wigner functions for the state of the probe at various points in the protocol, with colors denoting the quasiprobability.

infinitesimal random twists. Despite still being highly sensitive to dephasing, states prepared via random OAT can be prepared $\sim 1/\sqrt{N}$ faster than a GHZ state.

Bounds on Axis-Agnostic Sensing.—

Before introducing our protocol, we investigate the problem of axis-agnostic sensing from an information-theoretic perspective. Consider a system of N qubit sensors prepared in a pure probe state $\rho = |\psi\rangle\langle\psi|$, into which a small, unknown rotation angle θ is encoded via the unitary $R_{\hat{n}}(\theta) = \exp(-iS_{\hat{n}}\theta)$ specified by an unknown rotation axis \hat{n} , where $S_{\hat{n}} := \mathbf{S} \cdot \hat{n}$ and $\mathbf{S} = (S_x, S_y, S_z)$ are the $SU(2)$ angular momentum operators for spin $S = N/2$.

For a given rotation axis \hat{n} , the precision $\Delta\theta$ for estimating a rotation angle θ is bounded by the single-parameter quantum Cramér-Rao bound [32, 33]

$$\Delta\theta \geq \frac{1}{\sqrt{\nu \mathcal{F}_{\hat{n}}(\theta)}}, \quad (1)$$

where ν is the number of shots and $\mathcal{F}_{\hat{n}}(\theta) := 4\text{Var}(S_{\hat{n}})$ is the Quantum Fisher Information (QFI). Equation (1) is saturable asymptotically

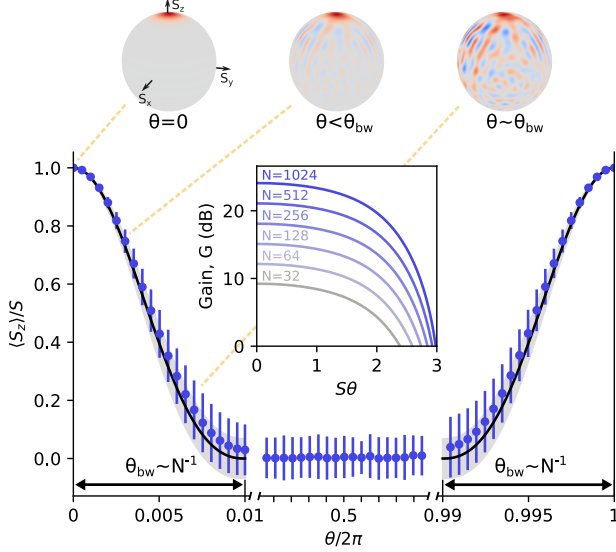


FIG. 2. **Spin polarization signal** $\langle S_z \rangle / S$ for $N = 100$ spins and 8 random OAT steps, each with twisting strength $\sim 1/\sqrt{N}$. Numerical simulations, averaged over 100 circuit realizations with a fixed rotation axis $\hat{n} = \hat{y}$, and analytic calculations (solid black) show a sharply decaying spin polarization signal as a function of θ , with a useful metrological bandwidth scaling like $\theta_{\text{bw}} \sim N^{-1}$. Shot-to-shot FWHM fluctuations in the signal (numerics in blue, analytics in grey) are subleading in the large- N limit. Inset: Metrological gain for $N = 32, 64, \dots, 1024$ as a function of rotation angle within the bandwidth.

in ν . One can show that $\mathcal{F}_{\hat{n}}(\theta) \leq N^2$, and protocols achieving this scaling with N are called Heisenberg-limited. As knowing \hat{n} can only improve estimation precision, any protocol for an *unknown* rotation axis that manages to obtain this scaling must be optimal, up to constant factors.

Under certain conditions this scaling is indeed obtainable. In particular, for single-shot or non-adaptive estimation, the encoding procedure $\rho \mapsto \rho_\theta$ for an unknown rotation axis \hat{n} can be written as a mixed-unitary quantum channel

$$\rho_\theta = \mathcal{M}_\theta[\rho] := \mathbb{E}_{\hat{n}} \left[R_{\hat{n}}(\theta) \rho R_{\hat{n}}^\dagger(\theta) \right]. \quad (2)$$

As detailed in Section S1 of supplemental material (SM), for small θ , this channel can be expressed as a depolarizing channel [34], for which we can compute the quantum Fisher information. We find that, at leading order in θ , Heisenberg scaling is achievable.

Butterfly Echo Protocol.—We now introduce the butterfly echo protocol that achieves axis-agnostic Heisenberg scaling and summarize its steps in Fig. 1.

Step 1 (Preparation): Starting from a completely polarized Dicke state $|S, S\rangle$, prepare the scrambled probe state $|\psi\rangle = U|S, S\rangle$ where U is a strongly-scrambling unitary acting on the symmetric subspace \mathcal{S}_N .

Step 2 (Encoding): Apply the rotation $R_{\hat{n}}(\theta)$ for unknown \hat{n} yielding the state $R_{\hat{n}}(\theta)|\psi\rangle$.

Step 3 (Measurement): Unscramble the state via time reversal yielding $U^\dagger R_{\hat{n}}(\theta)U|S, S\rangle$ and measure the spin polarization $\langle S_z \rangle$.

For vanishing rotation angle $\theta = 0$, the forward and backward time evolution cancel, and we are left with the original Dicke state $|S, S\rangle$ with maximal spin polarization $\langle S_z \rangle = S$. A non-vanishing rotation angle $\theta > 0$ leads to imperfect time-reversal and a commensurate reduction in the spin polarization $\langle S_z \rangle < S$, which serves as our metrological signal for the rotation angle θ , as shown in Fig. 2.

Scrambling within the symmetric subspace \mathcal{S}_N plays a crucial role in this protocol. For unitaries U drawn from a 2-design over \mathcal{S}_N , the butterfly echo protocol yields an angular sensitivity

$$\frac{1}{\Delta\theta} := \left. \frac{\partial (S - \overline{\langle S_z \rangle}) / \partial\theta}{\Delta S_z} \right|_{\theta=0} = \frac{N}{2} + \mathcal{O}(1), \quad (3)$$

where the bar indicates Haar-averaged quantities and the $\mathcal{O}(1)$ terms are subleading for large N [35]. Equation (3) differs from optimality by only a factor of $2/\sqrt{3}$ [36]. Furthermore, if the scrambling unitaries come from a 4-design over \mathcal{S}_N , the variance in the QFI due to different circuit realizations scales as

$$\text{Var}_U [\mathcal{F}_{\hat{n}}(\theta)] = \frac{4}{45} N^3 + \mathcal{O}(N^2) \quad (4)$$

at large N , giving a standard deviation $\sim N^{3/2}$ that is subleading relative to the mean QFI $\sim N^2$. These analytical results allow us to quantify the metrological gain $G := 10 \log_{10}(1/(N\Delta\theta^2))$ (inset of Figure 2), which shows Heisenberg scaling for angles $\theta < \theta_{\text{bw}} \sim N^{-1}$ inside the bandwidth.

Intuitively, the probe states used in the butterfly echo protocol can be viewed as randomized versions of the anticoherent probe states considered in previous literature on rotoensing [18, 23, 37]. A quantum state ρ is order- k anticoherent if $\langle \hat{S}_{\hat{n}}^t \rangle$ is independent of \hat{n} for all $t \leq k$ [23, 38], providing a notion of state isotropy. A high degree of anticoherence improves rotoensor precision because an isotropic distribution of features ensures consistently high sensitivity to arbitrary rotation axes. In contrast to anticoherence—a notion of isotropy of a single state—a quantum state k -design [39–41] over \mathcal{S}_N provides a notion of isotropy of an ensemble of states $\mathcal{E} \subseteq \mathcal{S}_N$. In particular, an ensemble \mathcal{E} is a state k -design if $\mathbb{E}_{\rho \in \mathcal{E}} [f_k(\rho)] = \overline{f_k(\rho)}$ for any degree- k polynomial $f_k(\rho)$, where the overbar indicates the Haar-average over states in \mathcal{S}_N . As detailed in Section S2, there is a sharp correspondence between the two notions of isotropy, providing intuition for the success of the butterfly echo protocol provided that the randomly prepared probe states form, at least approximately, a sufficiently high order symmetric state design.

Probe State Preparation.—While the ideal probe state is prepared using a symmetric unitary operator U sampled from the Haar ensemble, such an operator is extremely difficult to generate in realistic experiments. Here we show that low-depth chaotic random circuits suffice to generate approximate Haar-random unitary dynamics using only rotations and one-axis twisting (OAT) operations that are native to relevant experimental platforms including cavity QED [42], trapped ions [43], and NV centers [44]. Inspired by the canonical kicked top model [16, 45–47], we consider an ensemble of random one-axis twisting preparation circuits comprised of a series of one-axis twists $U_j = \exp(-i\chi t S_{\hat{m}_j}^2)$ performed along random axes \hat{m}_j at each timestep $j = \{1, 2, \dots\}$. For each timestep we apply a twisting strength $\chi t = \frac{\pi}{2\sqrt{N}}$ corresponding to the strength required to wrap a coherent state around the Bloch sphere once (see Fig. 3(a)).

These chaotic random circuits rapidly scramble the spin and generate approximately Haar-random probe states with Heisenberg-scaled per-

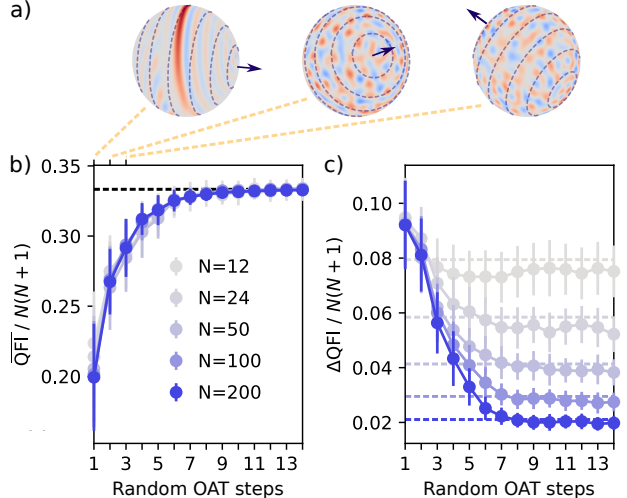


FIG. 3. **Probe state preparation** requires only a handful of random twists. Successive applications of random one-axis twisting dynamics yield approximately Haar-random states (a) with a mean QFI (b, dots) that rapidly approaches the ideal value $\overline{\text{QFI}} = N(N+1)/3$ (dashed) on a timescale that is independent of the system size N . Fluctuations in the QFI (c, dots) also converge to their Haar-random values (dashed) on the same timescale. Numerical data was averaged over 100 random OAT circuits (300 for $N = 12$) and 10^3 randomly-chosen rotation axes \hat{n} . Error bars are shrunk by a factor of 3 for visual clarity.

formance after only a handful of twisting operations (Fig. 3). Visual inspection of the Wigner functions at each timestep t (Fig. 3(a)) already provides an indication of convergence to Haar randomness. Direct calculation of the mean QFI—averaged over circuit realizations and rotation axes (Fig. 3(b), solid)—reveals rapid convergence to the ideal Haar-random value $N(N+1)/3$ (dashed). Crucially, the number of timesteps required for convergence is constant in the system size N (by contrast, preparing a GHZ state requires $\mathcal{O}(\sqrt{N})$ OAT steps). To verify this claim, we have also analytically studied a related infinitesimal random OAT model in which the twisting strength χt is taken to zero while the total circuit depth is kept fixed (see SM, Section S5). The ensemble-averaged effective Hamiltonian for this model features an energy gap that is constant with system size, indicating a timescale to convergence that does not depend on N .

While the mean QFI provides a measure of the *typical* metrological usefulness of probe states prepared by random OAT dynamics, one must also be concerned with the size of fluctuations around the mean due to different realizations of random preparation circuits. Numerical simulations (Fig. 3(c)) demonstrate rapid convergence of the standard deviation of the QFI (solid) to its Haar-random value $\Delta\text{QFI} = \frac{2N^{3/2}}{3\sqrt{5}}$ (dashed) on the same timescale as the convergence of the mean QFI. Again, the number of timesteps required for convergence does not depend on the system size N .

Effects of Decoherence.—With an eye toward experimental implementation, we study the sensitivity of the butterfly echo protocol to collective and single-particle dephasing. Analytic calculations combining random matrix theory and degenerate perturbation theory (SM, Section S4) yield an analytic expression for the metrological gain in the presence of collective dephasing at a rate γ_c (Fig. 4(a)). Although dissipation completely destroys the metrological gain at vanishingly small rotation angles $\theta \sim 0$, we still find sensitivities surpassing the standard quantum limit for a substantial fraction of the bandwidth θ_{bw} up to collective dephasing rates of $\gamma_c \sim \chi N^{-3/2} \times \mathcal{O}(1)$. The rotation angle for which the metrological gain is maximal is located at roughly half the bandwidth, which makes intuitive sense given that the signal $\langle S_z \rangle$ has its steepest slope at around $\theta \sim \theta_{\text{bw}}/2$.

We observe qualitatively identical behavior for increasing levels of single-particle dephasing, γ_s . Because such a process destroys the symmetry of the state, we limit our analysis to a few-body simulation using Permutation Invariant Quantum Solver from QuTiP [48]. The numerical results in Fig. 4b reveal that our protocol is more resilient to single-particle dephasing than collective dephasing.

The requirements on dephasing rates are strict, and they further tighten with an increase in particle number, N . Nevertheless, the butterfly echo protocol can still lead to a practical advantage in magnetometric rotosensing with high-spin lanthanide atoms, such as dysprosium-164. Tensor-light-shift-enabled OAT in dysprosium

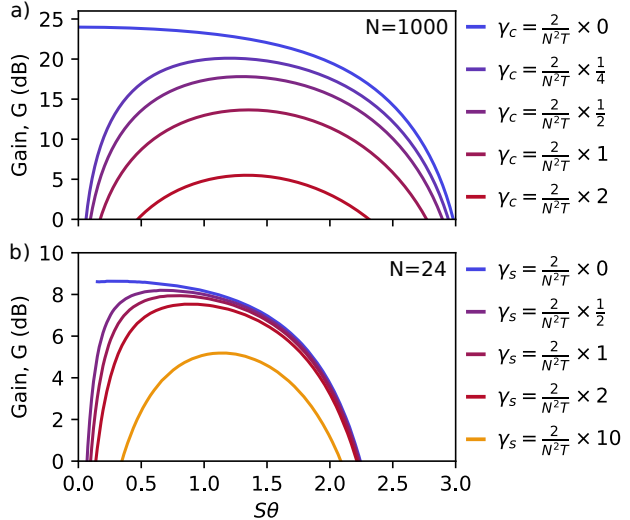


FIG. 4. **Decoherence reduces gain and bandwidth** of the butterfly echo protocol. We consider increasing rates of (a) collective and (b) single-particle dephasing, expressed in terms of the system size, N , and the total random one-axis twisting evolution time $T \sim \frac{\pi}{2\chi\sqrt{N}} \times \mathcal{O}(1)$. The results in (a) are analytic for $N = 10^3$ and scale universally with N , whereas the results in (b) are numerical for $N = 24$ and $T = \frac{\pi}{2\chi\sqrt{N}} \times 8$.

produced intrinsic spin squeezing, as well as intrinsic non-Gaussian [49] and GHZ states [50], proving sufficient levels of coherence for our protocol to be effective.

Outlook.—Although the random OAT model is capable of generating sufficiently random scrambling unitaries in constant time, recent results in the study of unitary k -designs indicate that there may be more efficient methods to prepare the necessary probe states [51–53]. Further, without the information about the scrambling unitary used to prepare the probe state, end-users of our protocol retain zero knowledge about the rotation axis \hat{n} . This ability to effectively hide the rotation axis from users could be leveraged in double-blind inertial navigation protocols and suggests deeper connections between metrology, scrambling, and cryptography. We leave these interesting questions for future work.

Acknowledgments.—We thank Brian Swingle for helpful discussions early in the development of this work. We also thank Irina

Novikova for helpful discussions regarding the echo protocol's robustness to decoherence. JB notes that the views expressed in this work are those of the author and do not reflect the official policy or position of the United States Naval Academy or any department of the United States Government. L.Z., M.R., A.V.G., and V.V. acknowledge support from the U.S. Department of Energy, Office of Science, National Quantum Information Science Research Centers, Quantum Systems Accelerator (award No. DE-SCL0000121). A.V.G. was also supported in part by ONR MURI, ARL (W911NF-24-2-0107), the DoE ASCR Quantum Testbed Pathfinder program (award No. DE-SC0024220), NSF QLCI (award No. OMA-2120757), NSF STAQ program, AFOSR MURI, DARPA SAVaNT ADVENT, and NQVL:QSTD:Pilot:FTL. A.V.G. also acknowledges support from the U.S. Department of Energy, Office of Science, Accelerated Research in Quantum Computing, Fundamental Algorithmic Research toward Quantum Utility (FAR-Qu).

Note added: *In the final stages of preparation of this manuscript, Ref. [54] was posted on arXiv, presenting numerical results on a similar echo-based protocol. Their results are consistent with ours.*

* These authors contributed equally to this work.

- [1] G. Tóth and I. Apellaniz, *J. Phys. A: Math. Theor.* **47**, 424006 (2014).
- [2] T. Kielinski, P. O. Schmidt, and K. Hammerer, *Sci. Adv.* **10**, eadr1439 (2024).
- [3] P. Niroula, J. Dolde, X. Zheng, J. Bringewatt, A. Ehrenberg, K. C. Cox, J. Thompson, M. J. Gullans, S. Kolkowitz, and A. V. Gorshkov, *Phys. Rev. Lett.* **133**, 080801 (2024).
- [4] M. Kitagawa and M. Ueda, *Phys. Rev. A* **47**, 5138 (1993).
- [5] D. J. Wineland, J. J. Bollinger, W. M. Itano, and D. J. Heinzen, *Phys. Rev. A* **50**, 67 (1994).
- [6] V. Giovannetti, S. Lloyd, and L. Maccone, *Science* **306**, 1330 (2004).
- [7] L. Maccone and A. Ricciardi, *Quantum* **4**, 292 (2020).
- [8] E. Davis, G. Bentsen, and M. Schleier-Smith, *Phys. Rev. Lett.* **116**, 053601 (2016).
- [9] T. Macrì, A. Smerzi, and L. Pezzè, *Phys. Rev. A* **94**, 010102 (2016).
- [10] D. Linnemann, H. Strobel, W. Muessel, J. Schulz, R. J. Lewis-Swan, K. V. Kheruntsyan, and M. K. Oberthaler, *Phys. Rev. Lett.* **117**, 013001 (2016).
- [11] O. Hosten, R. Krishnakumar, N. J. Engelsen, and M. A. Kasevich, *Science* **352**, 1552 (2016).
- [12] S. P. Nolan, S. S. Szigeti, and S. A. Haine, *Phys. Rev. Lett.* **119**, 193601 (2017).
- [13] S. Colombo, E. Pedrozo-Penafiel, A. F. Adiyatullin, Z. Li, E. Mendez, C. Shu, and V. Vuletić, *Nat. Phys.* **18**, 925 (2022).
- [14] M. Koppenhöfer, P. Groszkowski, and A. A. Clerk, *Phys. Rev. Lett.* **131**, 060802 (2023).
- [15] P. Chen and J. Jing, *Phys. Rev. A* **110**, 062425 (2024).
- [16] L. J. Fiderer and D. Braun, *Nat. Comm.* **9**, 1351 (2018).
- [17] B. Kobrin, T. Schuster, M. Block, W. Wu, B. Mitchell, E. Davis, and N. Y. Yao, *arXiv preprint arXiv:2411.12794* (2024).
- [18] C. Chryssomalakos and H. Hernández-Coronado, *Phys. Rev. A* **95**, 052125 (2017).
- [19] Y. Mo and G. Chiribella, *New J. Phys.* **21**, 113003 (2019).
- [20] A. Z. Goldberg, A. B. Klimov, G. Leuchs, and L. L. Sánchez-Soto, *J Phys. Photonics* **3**, 022008 (2021).
- [21] M. Cerdonio, G. A. Prodi, and S. Vitale, *General relativity and gravitation* **20**, 83 (1988).
- [22] P. Kolenderski and R. Demkowicz-Dobrzanski, *Phys. Rev. A* **78**, 052333 (2008).
- [23] J. Martin, S. Weigert, and O. Giraud, *Quantum* **4**, 285 (2020).
- [24] C. Chryssomalakos, L. Hanotel, E. Guzmán-González, D. Braun, E. Serrano-Ensástiga, and K. Życzkowski, *Phys. Rev. A* **104**, 012407 (2021).
- [25] F. Bouchard, P. de la Hoz, G. Björk, R. Boyd, M. Grassl, Z. Hradil, E. Karimi, A. Klimov, G. Leuchs, J. Řeháček, *et al.*, *Optica* **4**, 1429 (2017).
- [26] E. Serrano-Ensástiga, C. Chryssomalakos, and J. Martin, *Phys. Rev. A* **111**, 022435 (2025).
- [27] J. Denis, C. Read, and J. Martin, *SciPost Physics Core* **9**, 001 (2026).
- [28] I. Apellaniz, B. Lücke, J. Peise, C. Klempt, and G. Tóth, *New J. Phys.* **17**, 083027 (2015).
- [29] M. Oszmaniec, R. Augusiak, C. Gogolin, J. Kołodyński, A. Acín, and M. Lewenstein, *Phys. Rev. X* **6**, 041044 (2016).
- [30] J. Denis and J. Martin, *Phys. Rev. Res.* **4**, 013178 (2022).
- [31] G. S. Agarwal and L. Davidovich, *Phys. Rev.*

- Res. **4**, L012014 (2022).
- [32] C. W. Helstrom, *Quantum detection and estimation theory*, Vol. 3 (Academic press New York, 1976).
- [33] J. Liu, H. Yuan, X.-M. Lu, and X. Wang, *J. Phys. A: Math. Theor.* **53**, 023001 (2020).
- [34] A. Rivas and A. Luis, *Phys. Rev. A* **88**, 052120 (2013).
- [35] B. Collins, S. Matsumoto, and J. Novak, *Notices of the American Mathematical Society* **69**, 1 (2022).
- [36] M. G. Paris, *Int. J. Quantum Inf.* **7**, 125 (2009).
- [37] A. Z. Goldberg and D. F. V. James, *Phys. Rev. A* **98**, 032113 (2018).
- [38] J. Zimba, *EJTP* **3**, 143 (2006).
- [39] A. Ambainis and J. Emerson, in *Twenty-Second Annual IEEE Conference on Computational Complexity (CCC'07)* (IEEE, 2007) pp. 129–140.
- [40] D. Gross, K. Audenaert, and J. Eisert, *Journal of mathematical physics* **48** (2007).
- [41] D. A. Roberts and B. Yoshida, *Journal of High Energy Physics* **2017**, 1 (2017).
- [42] I. D. Leroux, M. H. Schleier-Smith, and V. Vuletić, *Phys. Rev. Lett.* **104**, 073602 (2010).
- [43] J. G. Bohnet, B. C. Sawyer, J. W. Britton, M. L. Wall, A. M. Rey, M. Foss-Feig, and J. J. Bollinger, *Science* **352**, 1297 (2016).
- [44] W. Wu, E. J. Davis, L. B. Hughes, B. Ye, Z. Wang, D. Kufel, T. Ono, S. A. Meynell, M. Block, C. Liu, H. Yang, A. C. Bleszynski Jayich, and N. Y. Yao, *Nature* **646**, 74 (2025).
- [45] F. Haake, M. Kuś, and R. Scharf, *Zeitschrift für Physik B Condensed Matter* **65**, 381 (1987).
- [46] C. Yin and A. Lucas, *Phys. Rev. A* **103**, 042414 (2021).
- [47] X.-Q. Wang, J. Ma, X.-H. Zhang, and X.-G. Wang, *Chin. Phys. B* **20**, 050510 (2011).
- [48] N. Shammah, S. Ahmed, N. Lambert, S. De Liberato, and F. Nori, *Phys. Rev. A* **98**, 063815 (2018).
- [49] A. Evrard, V. Makhalov, T. Chalopin, L. A. Sidorenkov, J. Dalibard, R. Lopes, and S. Nascimbene, *Phys. Rev. Lett.* **122**, 173601 (2019).
- [50] T. Chalopin, C. Bouazza, A. Evrard, V. Makhalov, D. Dreon, J. Dalibard, L. A. Sidorenkov, and S. Nascimbene, *Nat. Comm.* **9**, 4955 (2018).
- [51] N. LaRacuenta and F. Leditzky, *arXiv preprint arXiv:2407.07876* (2024).
- [52] T. Schuster, J. Haferkamp, and H.-Y. Huang, *Science* **389**, 92 (2025).
- [53] L. Grevink, J. Haferkamp, M. Heinrich, J. Helsen, M. Hinsche, T. Schuster, and Z. Zimborás, *arXiv preprint arXiv:2506.23925* (2025).
- [54] D.-S. Liu, Z.-J. Chen, Z. Hua, Y. Zhou, Q.-X. Jie, W. Cai, M. Li, L. Sun, C.-L. Zou, X.-F. Ren, *et al.*, *arXiv preprint arXiv:2601.16026* (2026).
- [55] M.-D. Choi, *Linear Algebra Its Appl.* **10**, 285 (1975).
- [56] A. Jamiołkowski, *Rep. Math. Phys.* **3**, 275 (1972).
- [57] G. S. Bentsen, S. Sahu, and B. Swingle, *Phys. Rev. B* **104**, 094304 (2021).
- [58] S. Personick, *IEEE Transactions on Information Theory* **17**, 240 (1971).

Supplemental Material

In this supplemental material we elaborate on the details of the calculations described in the main text. In particular, in Section S1 we show how the mixed unitary channel in Eq. (2) of the main text, describing rotation about an unknown axis, can be expressed as a depolarizing channel. We then compute the quantum Fisher information for this channel, indicating that Heisenberg scaling is, indeed, possible for the rotosensing problem. In Section S2 we elaborate on the connection between the anticonherent states that have previously been studied in the context of the rotosensing problem and quantum state designs over the symmetric space \mathcal{S}_N . In Section S3 we provide the details of the random matrix analysis that rigorously demonstrate the performance of our butterfly echo protocol when using Haar random symmetric states. In Section S4 we provide details for the analytic calculation of the effects of collective dephasing on the butterfly echo protocol. In Section S5 we analyze a Brownian circuit model for generating random symmetric probe states and show that it is equivalent to the random OAT model for preparing probe states in the limit of infinitesimal twists. Examining the spectrum of the effective Hamiltonian that describes this model indicates that the timescale to reach a metrologically useful Haar-random probe state is constant in system size. Finally, in Section S6 we compare our estimation scheme (measuring S_z) to the minimum mean square error (MMSE) estimator that is optimal from a Bayesian approach to analyzing the rotosensing problem.

S1. MIXED UNITARY CHANNEL FORM OF THE UNKNOWN AXIS PROBLEM

From Mixed Unitary Channel to Depolarizing Channel

In this section, we show that the mixed-unitary channel in Eq. (2) describing the encoding procedure for the rotosensing problem can be expressed as a depolarizing channel. In particular, any non-adaptive scheme or when operating in the single-shot regime, a rotosensing protocol must be rotation-axis agnostic. Thus, as described in the main text we can consider the encoding procedure as a mixed-unitary quantum channel

$$\begin{aligned}\rho_\theta &= \mathcal{M}_\theta[\rho] := \int d\hat{n} p(\hat{n}) R_{\hat{n}}(\theta) \rho R_{\hat{n}}^\dagger(\theta) \\ &= \frac{1}{4\pi} \int d\hat{n} R_{\hat{n}}(\theta) |\psi\rangle \langle \psi| R_{\hat{n}}^\dagger(\theta)\end{aligned}\quad (\text{S1})$$

where $p(\hat{n})$ is our prior distribution for the unknown rotation axis, which we take to be a uniform distribution, $\rho = |\psi\rangle \langle \psi|$ is the probe state, and $R_{\hat{n}}(\theta)$ is a unitary rotation about the axis \hat{n} by angle θ .

For small θ we can write the mixed-unitary channel in Eq. (S1) in a somewhat simpler form,

$$\mathcal{M}_\theta[\rho] = \rho + \mathcal{D}_\theta[\rho] + \mathcal{O}(\theta^3), \quad (\text{S2})$$

where $\mathcal{D}_\theta[\rho]$ is the depolarizing channel

$$\mathcal{D}_\theta[\rho] := \frac{\theta^2}{3} \sum_{j \in \{x, y, z\}} \left(S_j \rho S_j - \frac{1}{2} \{S_j^2, \rho\} \right) \quad (\text{S3})$$

To see this, simply expand Eq. (S1) to second order in θ :

$$\begin{aligned}\mathcal{M}_\theta[\rho] &= \rho + \frac{1}{4\pi} \int d\hat{n} [-i\hat{n} \cdot \mathbf{S} \rho + i\rho \hat{n} \cdot \mathbf{S}] \theta \\ &\quad + \frac{1}{4\pi} \int d\hat{n} \left[(\hat{n} \cdot \mathbf{S}) \rho (\hat{n} \cdot \mathbf{S}) - \frac{1}{2} \rho (\hat{n} \cdot \mathbf{S})^2 - \frac{1}{2} (\hat{n} \cdot \mathbf{S})^2 \rho \right] \theta^2 + \mathcal{O}(\theta^3).\end{aligned}\quad (\text{S4})$$

Using spherical harmonics it is straightforward to show that

$$\int d\hat{n} \hat{n} = 0, \quad (\text{S5a})$$

$$\int d\hat{n} \hat{n}_i \hat{n}_j = \frac{4\pi}{3} \delta_{ij}, \quad (\text{S5b})$$

so the terms linear in θ vanish and we obtain Eq. (S2).

Quantum Fisher Information for the Depolarizing Channel

Now that we have reduced the problem of learning a small rotation θ about an unknown axis to estimating the strength of a depolarization channel $\mathcal{M}_\theta[\rho] := \rho + \mathcal{D}_\theta[\rho] + \mathcal{O}(\theta^3)$, we compute the quantum Fisher information for this channel.

For small θ , the quantum Fisher information can be expressed as

$$\theta^2 \mathcal{F}(\theta) = 8 \left(1 - \sqrt{f(\rho, \mathcal{M}_\theta[\rho])} \right), \quad (\text{S6})$$

where

$$f(\rho, \sigma) = \text{Tr} \left[\sqrt{\sqrt{\rho} \sigma \sqrt{\rho}} \right]^2, \quad (\text{S7})$$

is the fidelity. For a pure probe state $\rho = |\psi\rangle\langle\psi| = \rho^2$, one finds that

$$\begin{aligned} f(\rho, \mathcal{M}_\theta[\rho]) &= \text{Tr} \left[\sqrt{\rho + \frac{\theta^2}{3} \left(\sum_j \langle S_j \rangle^2 \rho - \langle S_j^2 \rangle \rho \right) + \mathcal{O}(\theta^3)} \right]^2 \\ &= \text{Tr} \left[\rho \sqrt{1 + \frac{\theta^2}{3} \left(\sum_j \langle S_j \rangle^2 - \langle S_j^2 \rangle \right) + \mathcal{O}(\theta^3)} \right]^2 \\ &= \left[1 - \frac{\theta^2}{6} \sum_j \text{Var}(S_j) + \mathcal{O}(\theta^3) \right]^2. \end{aligned} \quad (\text{S8})$$

Thus,

$$\mathcal{F}(\theta) = \frac{4}{3} \sum_j \text{Var}(S_j) + \mathcal{O}(\theta^3). \quad (\text{S9})$$

Thus, for a Haar random symmetric probe state, the expectation value of the quantum Fisher information is

$$\overline{\mathcal{F}(\theta)} = \frac{4}{3} S(S+1) + \mathcal{O}(\theta) \sim S^2, \quad (\text{S10})$$

where we use Eq. (S17) from Sect. S3. The quantum Cramér-Rao bound implies that the signal to noise ratio R (for a single measurement) using a Haar random symmetric state is bounded (on average) as [36]

$$R^2 := \frac{\theta^2}{\text{Var}(\tilde{\theta})} \leq \theta^2 \overline{\mathcal{F}(\theta)} \sim \theta^2 S^2 \quad (\text{S11})$$

The butterfly-echo protocol yields an average signal-to-noise ratio $R \sim S\theta$, consistent with the optimal scaling as determined via the quantum Cramér-Rao bound.

S2. ANTICOHERENCE VERSUS SYMMETRIC STATE DESIGNS

In the section, we elaborate on the connections between anticomherent states and symmetric quantum state designs. As described in the main text, both are, in some sense, isotropic (with respect to the rotation axis \hat{n}). However, while anticomherence is a property of a single state, a symmetric state design is an ensemble of states.

A quantum state ρ is order- k anticomherent if $\langle \hat{S}_{\hat{n}}^t \rangle$ is independent of \hat{n} for all $t \leq k$ [23, 38]. Thus, the order of anticomherence specifies the extent of isotropy of a state: a higher order anticomherent state requires looking at expectation values of higher moments of spin operators to see any anisotropy. From this definition and the expression for the quantum Fisher information for rotation about a known axis \hat{n} ,

$$\mathcal{F}_{\hat{n}}(\theta) := 4(\Delta S_{\hat{n}})^2 = 4 \left[\langle S_{\hat{n}}^2 \rangle - \langle \hat{S}_{\hat{n}} \rangle^2 \right], \quad (\text{S12})$$

it follows that an order-2 anticomherent state provides Heisenberg scaling $\sim S^2$ for measuring a rotation about any *known* axis [37].

When considering rotosensing with an unknown axis, it is standard practice to examine the fidelity of the rotated state with the probe state averaged over \hat{n} ; with this figure of merit (which implies a particular choice of \hat{n} -independent measurement), higher order anticomherence always improves the sensitivity of the rotosensor [18, 23].

Recall that a symmetric quantum state k -design is an ensemble of states $\mathcal{E} \subseteq \mathcal{S}_N$ such that $\overline{f_k(\rho)} = \mathbb{E}_{\rho \in \mathcal{E}} [f_k(\rho)]$, for any polynomial of degree k , $f_k(\rho)$, where the overbar indicates the Haar average. By the isotropy of the symmetric Haar ensemble, this definition implies, that $\overline{\prod_{j=1}^t \langle S_{\hat{n}}^{s_j} \rangle}$ is independent of \hat{n} for all $t \leq k$ and all $s_j \in \mathbb{Z}^+$.

Where anticomherence is a notion of isotropy of an individual state, quantified by the isotropy of spin moments, symmetric state designs provide a notion of isotropy of an ensemble of states, quantified by k -body correlators of arbitrary spin moments. Nonetheless, there is clearly a correspondence between the two notions of isotropy. For instance, where an order-2 anticomherent state implies an isotropic $\mathcal{F}_{\hat{n}}(\theta)$ with Heisenberg scaling, a state 2-design implies an isotropic ensemble-averaged QFI, $\overline{\mathcal{F}_{\hat{n}}(\theta)}$, with Heisenberg scaling. In this sense, a symmetric state k -design gives a notion of order- k anticomherence on average, providing intuition for the success of the butterfly echo protocol

S3. RANDOM MATRIX ANALYSIS FOR BUTTERFLY ECHO PROTOCOL

In this section, we provide the details of the rigorous analysis of the butterfly echo protocol using random matrix theory. We initialize the system in the completely polarized Dicke state $|S, S\rangle$ and prepare the probe state $|\psi\rangle = U|S, S\rangle$ by applying a random $D \times D$ unitary matrix U sampled from the Haar ensemble \mathcal{H} [35], where $D = 2S + 1$ is the Hilbert space dimension. Initially we will focus on the clean (noiseless) case where $\gamma = 0$, but in later sections we will generalize to account for depolarizing noise that acts during state preparation and time-reversal.

Expectation Values and Quantum Fisher Information: First Moment Analysis

Before considering the echo protocol, let us first prepare the probe state $|\psi\rangle$ and study ensemble-averaged expectation values

$$\overline{\langle \psi | \mathcal{O} | \psi \rangle} = \mathbb{E}_{U \sim \mathcal{H}} \left[\langle S, S | U^\dagger \mathcal{O} U | S, S \rangle \right] \quad (\text{S13})$$

where the overbar indicates an average over Haar random unitaries U and \mathcal{O} is an arbitrary operator acting on the symmetric Dicke subspace. Such quantities are categorized as first-moment ($k = 1$) quantities because they involve a single forward evolution U and a single backward evolution U^\dagger . Using the Choi-Jamiołkowski isomorphism (see Figure S1) and the Weingarten calculus, we find that expectation values are given by the trace

$$\overline{\langle \psi | \mathcal{O} | \psi \rangle} = \text{Tr}[\mathcal{O}] / D \quad (\text{S14})$$

where $D = 2S + 1$ is the dimension of the Hilbert space. In other words, ensemble-averaged expectation values are just the expectation values for a maximally mixed state $\rho = \mathbb{I}/D$. This makes sense because the ensemble average over random unitaries U generates a maximally mixed state:

$$\overline{U |S, S\rangle \langle S, S| U^\dagger} = \mathbb{I}/D. \quad (\text{S15})$$

In particular, the average spin polarization vanishes in all directions $\overline{\langle \psi | S_{\hat{n}} | \psi \rangle} = \text{Tr}[S_{\hat{n}}] / D = 0$ and the variance is isotropic in the spin axis \hat{n} :

$$\overline{\langle \psi | S_{\hat{n}}^2 | \psi \rangle} = \text{Tr}[S_{\hat{n}}^2] / D = \frac{1}{3} S(S + 1). \quad (\text{S16})$$

This calculation captures the metrological usefulness of the probe state $|\psi\rangle = U |S, S\rangle$ because the variance governs the quantum Fisher information (QFI):

$$\overline{\mathcal{F}_{\hat{n}}(\theta)} = 4\overline{\text{Var}[S_{\hat{n}}]} = \frac{1}{3} N(N + 1) \quad (\text{S17})$$

which differs from the Heisenberg limit by a factor of $1/3$. yielding Heisenberg-limited scaling $\sim N^2$. Getting the correct subleading term $N/3$ above actually requires a $k = 2$ calculation, which we turn to in the next section.

Note that Eq. (S17) only holds for pure states $|\psi\rangle$ whereas a more complicated expression applies for mixed states [33]. This may cause some confusion since we just mentioned the maximally mixed state in Eq. (S15). However the maximally mixed state only appears after averaging over the ensemble $U \sim \mathcal{H}$; prior to this averaging every probe state $|\psi\rangle$ is pure and we may therefore use the simple pure-state expression Eq. (S17) for the QFI.

Echo Protocol: Second Moment Analysis

Next we consider the butterfly echo protocol, which prepares the final state

$$|\chi\rangle = U^\dagger e^{-iS_{\hat{n}}\theta} U |S, S\rangle, \quad (\text{S18})$$

and we are interested in computing ensemble-averaged expectation values

$$\overline{\langle \chi | \mathcal{O} | \chi \rangle} = \mathbb{E}_{U \sim \mathcal{H}} \left[\langle S, S | U^\dagger e^{iS_{\hat{n}}\theta} U \mathcal{O} U^\dagger e^{-iS_{\hat{n}}\theta} U |S, S\rangle \right] \quad (\text{S19})$$

in this final state. Such quantities are categorized as second-moment ($k = 2$) quantities because they involve two pairs of forward and backward evolutions U, U^\dagger . Using the Choi-Jamiołkowski isomorphism (see Figure S1) and the Weingarten calculus, we find that expectation values are given by

$$\begin{aligned} \overline{\langle \chi | \mathcal{O} | \chi \rangle} &= \frac{1}{D^2 - 1} [f^2(\theta) \langle S, S | \mathcal{O} | S, S \rangle + D \text{Tr}[\mathcal{O}]] \\ &\quad - \frac{1}{D(D^2 - 1)} [f^2(\theta) \text{Tr}[\mathcal{O}] + D \langle S, S | \mathcal{O} | S, S \rangle] \\ &= \text{Tr}[\mathcal{O}] / D + \frac{1}{D^2 - 1} (f^2(\theta) - 1) (\langle S, S | \mathcal{O} | S, S \rangle - \text{Tr}[\mathcal{O}] / D) \end{aligned} \quad (\text{S20})$$

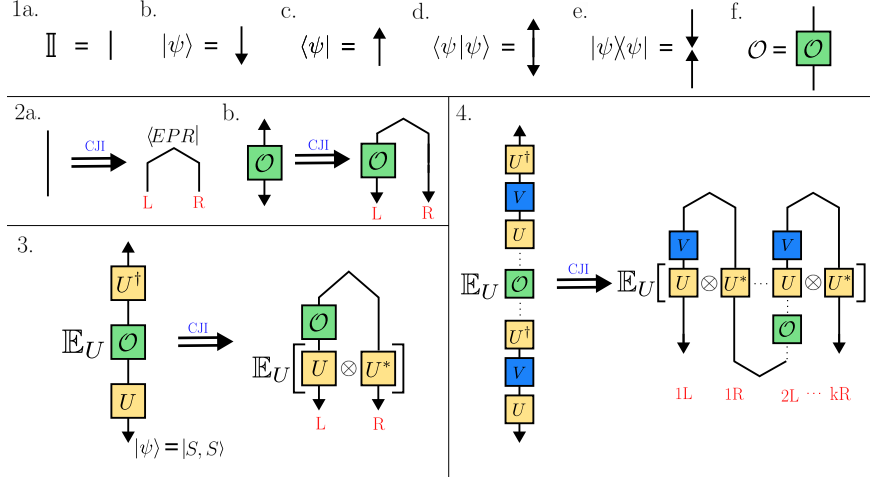


FIG. S1. Visual representation of the Choi-Jamiołkowski isomorphism (CJI) depicted using tensor-network notation. Notation is defined in panel 1 with: (1a) identity, (1b-c) states, (1d-e) products, and (1f) operators. The CJI acts turns the bras or kets that make up an operator into their counterpart. For instance (2a) shows the transformation on the identity for a spin-1/2 system, which maps $|0\rangle\langle 0| + |1\rangle\langle 1| \rightarrow \langle 0|_L \otimes \langle 0|_R + \langle 1|_L \otimes \langle 1|_R = \langle EPR|_{LR}$. (2b) shows how expectation values of operators on states transform under the isomorphism: $\langle\psi|\mathcal{O}|\psi\rangle \rightarrow \langle EPR|_{LR}(\mathcal{O}_L \otimes \mathbb{I}_R)|\psi\rangle_L \otimes |\psi\rangle_R$. (3) When taking expectation values averaged over Haar random unitaries U , we can use the CJI to isolate the U operators, absorbing any other operators into our boundary conditions. (4) shows a more complicated version of the same idea. Here, k is the number of pairs of replicas of U .

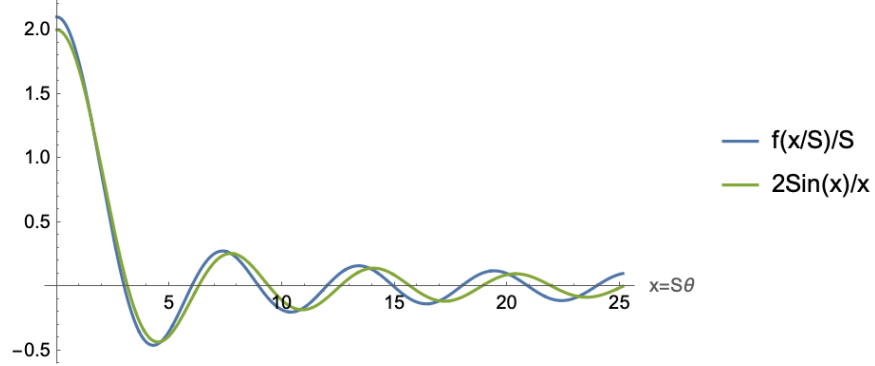


FIG. S2. The function $f(\theta)/S$ plotted versus $x = S\theta$ for $S = 10$ (blue) and its asymptotic large- S behavior (green).

where

$$f(\theta) = \text{Tr} \left[e^{-iS_n\theta} \right] = \sum_{m=-S}^S e^{-im\theta} = \cos(S\theta) + \cot(\theta/2) \sin(S\theta). \quad (\text{S21})$$

At large S and fixed $x = S\theta$, this function asymptotes to the sinc function:

$$\lim_{S \rightarrow \infty} f(x/S)/S = 2 \frac{\sin x}{x} \equiv 2 \text{sinc}(S\theta) \quad (\text{S22})$$

as shown in Fig. S2.

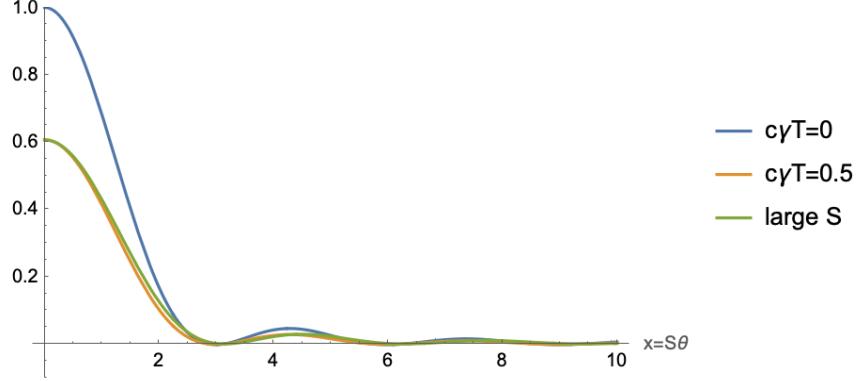


FIG. S3. The expected signal $\langle S_z \rangle / S = \overline{\langle \chi | S_z | \chi \rangle} / S$ as a function of $x = S\theta$ for $S = 10$ and $c\gamma T = 0$ (blue) and $c\gamma T = 0.5$ (orange). We also plot the asymptotic large- S behavior with $c\gamma T = 0.5$ (green).

We can use this expression to compute the metrological signal, which is governed by the expectation value of S_z :

$$\overline{\langle \chi | S_z | \chi \rangle} = \frac{S}{(2S+1)^2 - 1} [f^2(\theta) - 1]. \quad (\text{S23})$$

At large S and fixed $x = S\theta$ this asymptotes to:

$$\lim_{S \rightarrow \infty} \overline{\langle \chi | S_z | \chi \rangle} / S = \text{sinc}^2(S\theta) \quad (\text{S24})$$

as shown in Fig. S3. We can also use it to compute the noise in the signal caused by quantum fluctuations, which is governed by the expectation value of S_z^2 :

$$\overline{\langle \chi | S_z^2 | \chi \rangle} = \frac{1}{3} S(S+1) + \frac{(2S-1)}{12(S+1)} [f^2(\theta) - 1]. \quad (\text{S25})$$

At large S and fixed $x = S\theta$ this asymptotes to:

$$\lim_{S \rightarrow \infty} \overline{\langle \chi | S_z^2 | \chi \rangle} / S^2 = \frac{1}{3} [1 + 2 \text{sinc}^2(S\theta)] \quad (\text{S26})$$

as shown in Fig. S4. Putting this all together, we obtain an expression for the quantum fluctuations

$$\Delta S_z = \sqrt{\overline{\langle \chi | S_z^2 | \chi \rangle} - \overline{\langle \chi | S_z | \chi \rangle}^2} \quad (\text{S27})$$

which has asymptotic behavior

$$\lim_{S \rightarrow \infty} \Delta S_z / S = \frac{1}{\sqrt{3}} \sqrt{1 + 2 \text{sinc}^2(S\theta) - 3 \text{sinc}^4(S\theta)} \quad (\text{S28})$$

as shown in Fig. S5. Finally, we can combine these results to compute the angular sensitivity

$$\begin{aligned} \frac{1}{\Delta\theta} &= \frac{\partial (S - \overline{\langle \chi | S_z | \chi \rangle}) / \partial\theta}{\Delta S_z} \\ &\approx N \frac{\sqrt{3}}{x} \frac{\text{sinc}(x) (\text{sinc}(x) - \cos(x))}{\sqrt{1 + 2 \text{sinc}^2(x) - 3 \text{sinc}^4(x)}} + \mathcal{O}(1) \\ &\approx \frac{N}{2} (1 - 3x^2/40 + \mathcal{O}(x^4)) + \mathcal{O}(1) \end{aligned} \quad (\text{S29})$$

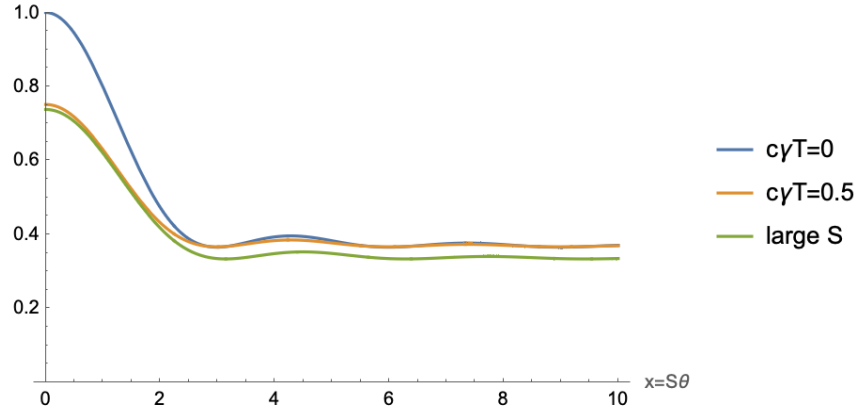


FIG. S4. The expectation value $\langle S_z^2 \rangle / S^2 = \overline{\langle \chi | S_z^2 | \chi \rangle} / S^2$ as a function of $x = S\theta$ for $S = 10$ and $c\gamma T = 0$ (blue) and $c\gamma T = 0.5$ (orange). We also plot the asymptotic large- S behavior with $c\gamma T = 0.5$ (green).

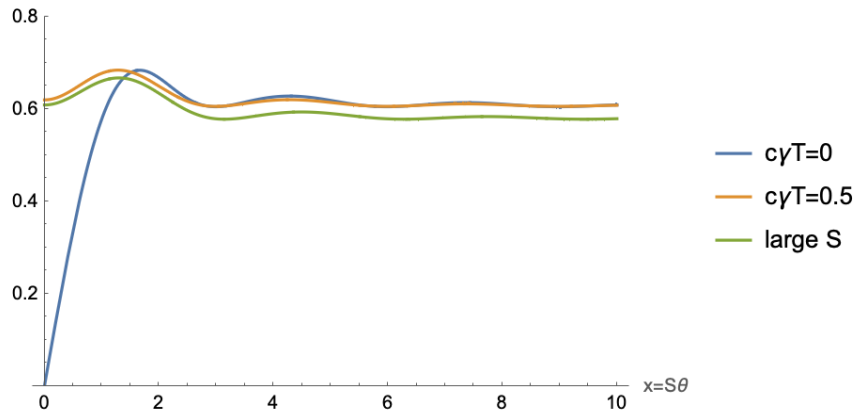


FIG. S5. Quantum fluctuations $\Delta S_z / S$ as a function of $x = S\theta$ for $S = 10$ and $c\gamma T = 0$ (blue) and $c\gamma T = 0.5$ (orange). We also plot the asymptotic large- S behavior with $c\gamma T = 0.5$ (green). Notice that the depolarizing noise has completely erased the linear behavior at small x observed in the clean case.

where we have truncated the expression to the leading term in the large N limit. We see that the angular sensitivity is sub-optimal near $x = 0$ by a factor of $\sqrt{3}/2 \approx 0.866$ compared to the angular sensitivity of $\Delta\theta^{-1} \approx N/\sqrt{3}$ that we expect from the Cramer-Rao bound and the quantum Fisher information of a random Dicke state. We plot the resulting metrological gain

$$G = 10 \log_{10} \left(\frac{1}{N\Delta\theta^2} \right) \quad (\text{S30})$$

in Figs. S6 and S7.

Bounding the Fluctuations: Second, Third, and Fourth Moment Analysis

Crucially, the random choice of unitary operators U will lead to fluctuations in the QFI $\mathcal{F}_{\hat{n}}(\theta)$ and the metrological signal $\langle S_z \rangle$. One might reasonably be concerned that this additional source of noise will overwhelm the metrological signal but we show here that these fluctuations are strictly smaller than the inherent quantum fluctuations. These fluctuations come in two flavors: for a fixed

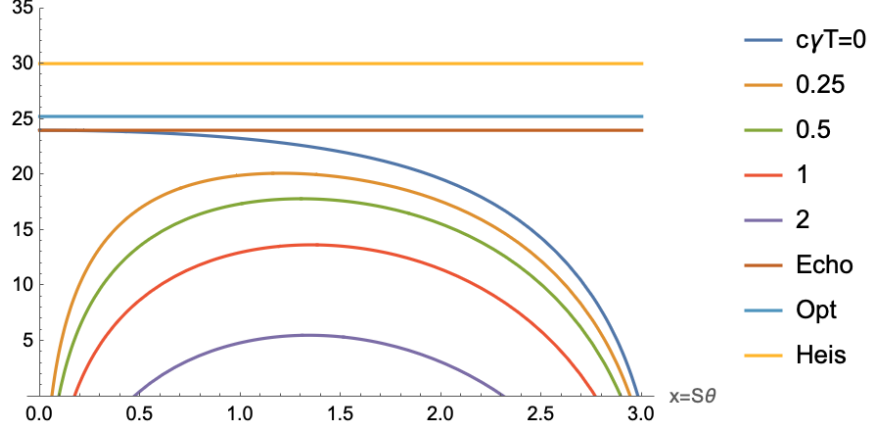


FIG. S6. Metrological gain G as a function of $x = S\theta$ for $N = 10^3$ and depolarizing noise $c\gamma T = 0, 0.25, 0.5, 1, 2$, compared to the maximum gain for the echo protocol (brown), the optimal gain for random Dicke states (light blue), and the Heisenberg limit (yellow).

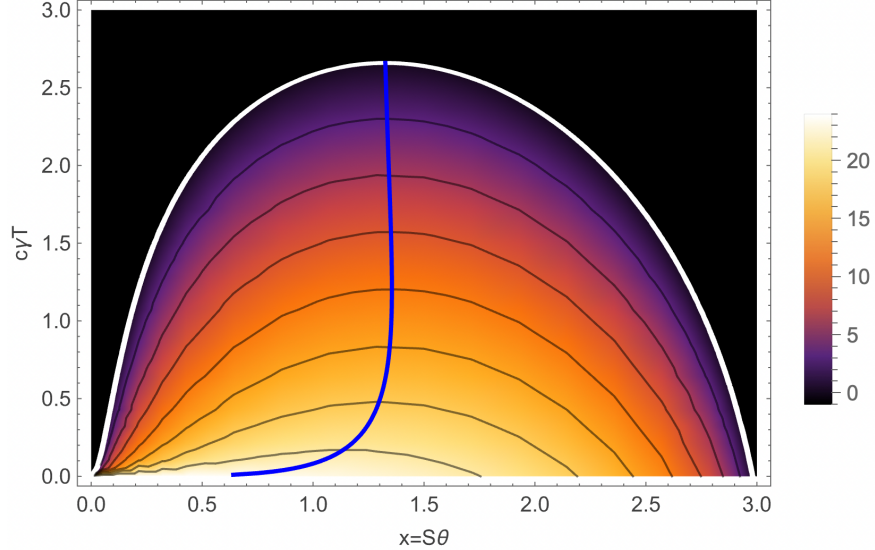


FIG. S7. Metrological gain G as a function of $x = S\theta$ and $c\gamma T$ for $N = 10^3$. Black contours are drawn at 3dB intervals and the blue curve shows the optimal sensing angle x^* as a function of noise $c\gamma T$. The black region indicates parameter regimes with no metrological gain and the white boundary illustrates the phenomenon of bandwidth narrowing.

rotation axis \hat{n} we expect to see shot-to-shot fluctuations in the QFI and the metrological signal as we vary the preparation unitary U . For the QFI, these fluctuations are captured by the variance

$$\text{Var}_U [\mathcal{F}_{\hat{n}}(\theta)] = \overline{\mathcal{F}^2} - \overline{\mathcal{F}}^2 = \overline{\text{Var}[S_{\hat{n}}]^2} - \overline{\text{Var}[S_{\hat{n}}]}^2 \quad (\text{S31})$$

where the first term involves contributions from moments $k = 2, 3, 4$ and the second term was computed earlier. For the metrological signal, these fluctuations are captured by the variance

$$\text{Var}_U [\langle \chi | S_z | \chi \rangle] = \overline{\langle \chi | S_z | \chi \rangle^2} - \left(\overline{\langle \chi | S_z | \chi \rangle} \right)^2 \quad (\text{S32})$$

where the first term contains contributions from the fourth moment $k = 4$ and the second term was computed earlier. Crucially, neither of these quantities depends on the rotation axis \hat{n} , so there is

no need to perform additional averaging over the rotation axis.

In addition to shot-to-shot fluctuations, for a fixed unitary U we expect to see anisotropic fluctuations in the signal as we vary the rotation axis \hat{n} . For the QFI, these fluctuations are captured by the variance

$$\overline{\text{Var}_{\hat{n}} [\mathcal{F}_{\hat{n}}(\theta)]} = \overline{\mathbb{E}_{\hat{n}} [\mathcal{F}_{\hat{n}}^2]} - \overline{\mathbb{E}_{\hat{n}} [\mathcal{F}_{\hat{n}}]^2} = \overline{\mathcal{F}^2} - \overline{\mathbb{E}_{\hat{n}, \hat{m}} [\overline{\mathcal{F}_{\hat{n}} \mathcal{F}_{\hat{m}}}]}$$
 (S33)

where we have exchanged the order of the averages over \hat{n}, U and dropped the \hat{n} average from the first term since the quantity does not depend on the rotation axis. The first term is the same as appeared above. For the second term we have explicitly written out the square of averages to emphasize that two different rotation axes \hat{n}, \hat{m} appear in the calculation. The second term involves moments $k = 2, 3, 4$. For the metrological signal, these anisotropic fluctuations are captured by the variance

$$\begin{aligned} \overline{\text{Var}_{\hat{n}} [\langle \chi | S_z | \chi \rangle]} &= \overline{\mathbb{E}_{\hat{n}} [\langle \chi | S_z | \chi \rangle_{\hat{n}}^2]} - \overline{\mathbb{E}_{\hat{n}} [\langle \chi | S_z | \chi \rangle_{\hat{n}}]^2} \\ &= \overline{\langle \chi | S_z | \chi \rangle^2} - \overline{\mathbb{E}_{\hat{n}, \hat{m}} [\langle \chi | S_z | \chi \rangle_{\hat{n}} \langle \chi | S_z | \chi \rangle_{\hat{m}}]} \end{aligned}$$
 (S34)

where the first term is the same as appeared above, and the second term involves a fourth moment $k = 4$ calculation.

In what follows we will use the Weingarten calculus to compute the leading order contributions in the large- S limit. Because the calculations of the various quantities of interest involve similar steps, we only discuss the calculation of the quantity

$$Q_{\hat{n}, \hat{m}} = \overline{\langle \chi | S_z | \chi \rangle_{\hat{n}} \langle \chi | S_z | \chi \rangle_{\hat{m}}}$$
 (S35)

in detail, and simply report the results for the other quantities above. Using the Choi-Jamiolkowski isomorphism, we may express the quantity $Q_{\hat{n}, \hat{m}}$ in terms of $2k$ replicas labeled by the indices $r = 1, 2, \dots, k$ and $a = L, R$ where L indicates a forward-time replica U and R indicates a backward-time replica U^T . Using the Weingarten calculus, the expectation value over the Haar ensemble yields a sum over all possible pairings of forward U and time-reversed U^T replicas, where each term in the sum is weighted by the Weingarten functions $\text{Wg}(\sigma\tau^{-1}, D)$ where $D = 2S + 1$ is the Hilbert space dimension [35]. For the present case we have $k = 4$, and σ, τ are elements of the symmetric group S_4 that parameterize the possible replica pairings. There are $|S_4| = 4! = 24$ possible elements, leading to a total of $(4!)^2 = 576$ terms, which we label by the tuple $[\sigma, \tau]$. Fortunately, most of these terms are subleading in the limit of large S , and our task in the following is to isolate only the leading-order terms and ignore the rest.

The leading term is the trivial pairing $[\sigma, \tau] = [\mathbb{I}, \mathbb{I}]$ where $\sigma = \tau = \mathbb{I} \equiv \mathbb{I}^4$ is the identity element, and the superscript reminds us that we are working with $k = 4$ and permutation elements $\sigma, \tau \in S_4$. This yields the leading $\mathcal{O}(S^2)$ contribution

$$\begin{aligned} &\text{Wg}(\mathbb{I}^4, D) \langle S, S | S_z | S, S \rangle^2 \text{Tr}^2 \left[e^{-iS_{\hat{n}}\theta} \right] \text{Tr}^2 \left[e^{-iS_{\hat{m}}\theta} \right] \\ &= \text{Wg}(\mathbb{I}^4, D) S^2 f^4(\theta) \quad [\mathbb{I}, \mathbb{I}] \end{aligned}$$
 (S36)

where the dependence on \hat{n}, \hat{m} disappears because the trace is axis-independent. Next we systematically identify all subleading terms of order $\mathcal{O}(S)$. There are two classes of terms that can appear: diagonal terms $[\sigma, \sigma]$, which always yield the leading-order Weingarten function $\text{Wg}(\sigma\sigma^{-1}, D) = \text{Wg}(\mathbb{I}^4, D)$; and off-diagonal terms $[\sigma, \tau]$ with $\sigma \neq \tau$, which yield subleading Weingarten functions $\text{Wg}(\sigma\tau^{-1}, D)$. We start with the diagonal terms; a direct search through all

$4! = 24$ possibilities yields the following 3 terms of order $\mathcal{O}(S)$:

$$\begin{aligned} 2\text{Wg}(\mathbb{I}^4, D)S^2f^2(\theta)f(\mu_+(\theta, \hat{n} \cdot \hat{m})) & \quad [(2\ 3), (2\ 3)] \text{ and } [(1\ 4), (1\ 4)] \\ 2\text{Wg}(\mathbb{I}^4, D)S^2f^2(\theta)f(\mu_-(\theta, \hat{n} \cdot \hat{m})) & \quad [(1\ 3), (1\ 3)] \text{ and } [(2\ 4), (2\ 4)] \\ \text{Wg}(\mathbb{I}^4, D)\frac{S(S+1)}{3}Df^2(\mu_+(\theta, \hat{n} \cdot \hat{m})) & \quad [(2\ 3)(1\ 4), (2\ 3)(1\ 4)] \end{aligned} \quad (\text{S37})$$

where $\sigma = (r\ s)$ is the transposition element that swaps replicas r, s . The transpositions (1 2) and (3 4) are absent from this list because the diagrams vanish exactly due to the fact that $\text{Tr}[S_z] = 0$. The angles μ_{\pm} originate in terms of the form

$$\text{Tr} \left[e^{-iS_{\hat{n}}\theta} e^{\pm iS_{\hat{m}}\theta} \right] = f(\mu_{\pm}(\theta, \hat{n} \cdot \hat{m})) \quad (\text{S38})$$

where the angles μ_{\pm} are given by the Rodrigues rotation formula

$$\cos \frac{\mu_{\pm}}{2} = \cos^2 \frac{\theta}{2} \pm (\hat{n} \cdot \hat{m}) \sin^2 \frac{\theta}{2}. \quad (\text{S39})$$

Note that the resulting expressions depend only on the rotation-invariant dot product $\hat{n} \cdot \hat{m}$, which makes sense because Haar-random averages are axis-independent.

Next we consider off-diagonal terms $[\sigma, \tau]$ with $\sigma \neq \tau$. To systematically identify the dominant terms, we take advantage of the fact that Weingarten functions $\text{Wg}(\sigma, D)$ are reduced by factors of $1/D$ for each additional transposition that appears in the transposition decomposition of σ . For example, $\text{Wg}(\mathbb{I}^4, D) \sim \mathcal{O}(D^{-4})$, whereas $\text{Wg}(2\mathbb{I}^2, D) \sim \mathcal{O}(D^{-5})$, where the notation $2\mathbb{I}^2$ indicates a single transposition of 2 elements while the other 2 elements are left unchanged. Hence, to conduct our search we first look for pairs of permutations σ, τ that differ by a single transposition. This yields the following 2 terms of order $\mathcal{O}(S)$:

$$\begin{aligned} 4\text{Wg}(2\mathbb{I}^2, D)S^2f^4(\theta) & \quad [\mathbb{I}, \sigma] \text{ for } \sigma = (2\ 3), (1\ 4), (2\ 4), (1\ 3) \\ 2\text{Wg}(2\mathbb{I}^2, D)\frac{S(S+1)}{3}Df^2(\theta)f(\mu_+(\theta, \hat{n} \cdot \hat{m})) & \quad [\sigma, (2\ 3)(1\ 4)] \text{ for } \sigma = (2\ 3), (1\ 4) \end{aligned} \quad (\text{S40})$$

where the transpositions $\sigma = (1\ 2), (3\ 4)$ do not appear in the first line because $\text{Tr}[S_z] = 0$. Finally, we find one remaining $\mathcal{O}(S)$ term generated by 2 pairs of transpositions:

$$\text{Wg}(2^2, D)\frac{S(S+1)}{3}Df^4(\theta) \quad [\mathbb{I}, (2\ 3)(1\ 4)] \quad (\text{S41})$$

Summing together all seven terms from Eqs. (S36), (S37), (S40), and (S41), we obtain an expression for $Q_{\hat{n}, \hat{m}}$ that is accurate to order $\mathcal{O}(S)$ for large S .

Finally we use these results to compute the leading order anisotropic variance in the metrological signal Eq. (S34). To do so we must take the expectation value over rotation axes \hat{n}, \hat{m} , which involves dealing with the functions $g(\mu_{\pm}) \equiv f(\mu_{\pm}(\theta, \hat{n} \cdot \hat{m})) / (2S + 1)$. Expanding Eq. (S34) to leading order in S we obtain

$$\frac{S}{6}\mathbb{E}_{\hat{n}, \hat{m}} \left[1 - g^2(\mu_+) + 4g^2(\theta) \left(1 - g(\mu_+) + \frac{3}{2}g(2\theta) - \frac{3}{2}g(\mu_-) \right) \right] \quad (\text{S42})$$

and expanding to leading order in $x = S\theta$ we obtain

$$\mathbb{E}_{\hat{n}, \hat{m}} \left[\frac{23}{270} (1 - (\hat{n} \cdot \hat{m})^2) Sx^4 + \mathcal{O}(x^6) \right] \quad (\text{S43})$$

which yields a variance of order

$$\overline{\text{Var}_{\hat{n}}[\langle\chi|S_z|\chi\rangle]} = \frac{23}{324}Sx^4 + S\mathcal{O}(x^6) \quad (\text{S44})$$

at lowest order in x and $1/S$. The same techniques can be used to compute the remaining variances above, which yield:

$$\text{Var}_U[\langle\chi|S_z|\chi\rangle] = \frac{17}{270}Sx^4 + S\mathcal{O}(x^6) \quad (\text{S45})$$

$$\text{Var}_U[\mathcal{F}_{\hat{n}}(\theta)] = \frac{4}{45}N^3 + \mathcal{O}(N^2) \quad (\text{S46})$$

All of these variances are subleading compared to the dominant quantum fluctuations.

S4. PERTURBATION THEORY FOR NOISY ECHO PROTOCOL

In this section we consider the effects of decoherence applied during state preparation and time-reversal. We assume an isotropic depolarizing channel described by the Lindblad master equation with jump operators $L_j = \sqrt{\gamma}S_j$ for $j = x, y, z$ where γ is the depolarizing rate. The Choi-Jamiołkowski isomorphism combined with disorder averaging [55–57] yield an effective Hamiltonian

$$H_{\text{eff},\gamma} = H_{\text{eff}} + \gamma V \quad (\text{S47})$$

where H_{eff} is the clean (noiseless) effective Hamiltonian obtained from the random OAT (or Brownian) model, and

$$V = \sum_{r=1}^k (S(S+1) + \mathbf{S}_{rL} \cdot \mathbf{S}_{rR}) \quad (\text{S48})$$

is the effective Hamiltonian generated by the depolarizing channel. Here we assume a perturbatively small depolarizing rate $\gamma \ll J$ and sufficiently large circuit depth $JT \gg 1$ such that the excited states of H_{eff} are not relevant to the long-time dynamics. In this case we can restrict our attention to the ground subspace and perform standard degenerate perturbation theory to compute the shifted ground states and their energies. The case $k = 1$ is trivial: in this case H_{eff} has a unique ground state $|\Omega\rangle$ which is also an exact eigenstate of V with vanishing eigenvalue, so the ground state $|\Omega\rangle$ is not shifted by V .

For $k = 2$ we have a 2-dimensional ground subspace spanned by the states $|\alpha\rangle, |\beta\rangle$ corresponding to the ‘ladder’ and ‘crossed’ saddle points, respectively. Note that these states are normalized but are *not orthogonal*:

$$\langle\alpha|\beta\rangle = \frac{1}{D} \quad (\text{S49})$$

To obtain an orthonormal basis for the ground subspace, we may use the standard Gram-Schmidt procedure to obtain

$$|\mu\rangle = \frac{D|\beta\rangle - |\alpha\rangle}{\sqrt{D^2 - 1}} \quad (\text{S50})$$

which guarantees $\langle \mu | \mu \rangle = 1$ and $\langle \mu | \alpha \rangle = 0$. We now apply standard degenerate perturbation theory, which involves computing matrix elements of V :

$$\begin{aligned}\langle \alpha | V | \alpha \rangle &= 0 \\ \langle \mu | V | \mu \rangle &= 2S(S+1) \frac{D^2}{D^2-1} \equiv c \\ \langle \alpha | V | \mu \rangle &= 0\end{aligned}\tag{S51}$$

Because the off-diagonal elements vanish, the eigenstates $|\alpha\rangle, |\mu\rangle$ themselves are not shifted as a result of the perturbation V . The only change is the first-order shift $c\gamma$ in the energy of $|\mu\rangle$.

These results allow us to generalize Eq. (S20) in the presence of dissipation. In the deep-circuit limit $JT \rightarrow \infty$ but where we keep γT fixed, we obtain

$$\overline{\langle \chi | \mathcal{O} | \chi \rangle} = \frac{D^2 - e^{-c\gamma T}}{D^2 - 1} \text{Tr}[\mathcal{O}] / D + \frac{e^{-c\gamma T}}{D^2 - 1} (f^2(\theta) - 1) (\langle S, S | \mathcal{O} | S, S \rangle - \text{Tr}[\mathcal{O}] / D)\tag{S52}$$

which we can immediately use to compute the metrological signal

$$\overline{\langle \chi | S_z | \chi \rangle} = \frac{S e^{-c\gamma T}}{D^2 - 1} [f^2(\theta) - 1].\tag{S53}$$

which decays exponentially with the circuit depth. Similarly, we can compute the second moment

$$\overline{\langle \chi | S_z^2 | \chi \rangle} = \frac{1}{3} S(S+1) \frac{D^2 - e^{-c\gamma T}}{D^2 - 1} + e^{-c\gamma T} \frac{(2S-1)}{12(S+1)} [f^2(\theta) - 1].\tag{S54}$$

At large S and fixed $x = S\theta$ this asymptotes to:

$$\lim_{S \rightarrow \infty} \overline{\langle \chi | S_z^2 | \chi \rangle} / S^2 = \frac{1}{3} [1 + e^{-c\gamma T} 2 \text{sinc}^2(S\theta)]\tag{S55}$$

which generalizes Eq. (S26). Combining these results we obtain the angular sensitivity

$$\begin{aligned}\frac{1}{\Delta\theta} &= \frac{\partial \left(S - \overline{\langle \chi | S_z | \chi \rangle} \right) / \partial\theta}{\Delta S_z} \\ &\approx N \frac{\sqrt{3}}{x} \frac{e^{-c\gamma T} \text{sinc}(x) (\text{sinc}(x) - \cos(x))}{\sqrt{1 + 2 \text{sinc}^2(x) e^{-c\gamma T} - 3 \text{sinc}^4(x) e^{-2c\gamma T}}} + \mathcal{O}(1)\end{aligned}\tag{S56}$$

where we have truncated the expression to the leading term in the large N limit. This expression generalizes Eq. (S29) to the noisy case. Eq. (S56) is one of our key technical contributions from the analytic calculations. We anticipate that at sufficiently large γ there is a phase transition in $H_{\text{eff},\gamma}$ to noise-dominated dynamics that are useless for metrology. We leave the study of this phase transition to future work.

S5. DERIVATION OF EFFECTIVE HAMILTONIAN SPECTRUM

In this section, we analyze a Brownian circuit model for generating random symmetric probe states and show that it is equivalent to the random one axis twisting (ROAT) model in the limit of infinitesimal twists. Using the Choi-Jamiołkowski isomorphism and disorder averaging [55–57] we can describe the circuit dynamics in terms of an effective Hamiltonian $H_{\text{eff}}^{(k)}$ where $2k$ is the

number of replicas (Fig. S1). Analysis of the spectrum of this effective Hamiltonian shows an energy gap that is constant in spin size S , indicating that the timescale required to reach the same metrological usefulness as a Haar-random probe state is constant in system size.

The main analysis performed was for the Brownian model, which will be shown later to have a proportional effective spectrum to the random OAT model given sufficiently small twisting times. Because of this, we elected to focus our computations primarily on the Brownian model. Defining our Brownian unitary as

$$U_B := \prod_t U_{B,t} = \prod_t \exp(-iH_B dt), \quad H_B := \sum_{\alpha\beta} J^{\alpha\beta}(t) S^\alpha S^\beta \quad (\text{S57})$$

where S represents our spin operator, α, β represent our defined axes, and $J^{\alpha\beta}(t)$ is the associated coupling coefficient, which we assume to be drawn from a Gaussian distribution with a mean of 0 and a variance of

$$\mathbb{E}_U[J^{\alpha\beta}(t)J^{\alpha'\beta'}(t')] := \frac{J\delta^{tt'}}{S^2 dt}(\delta^{\alpha\alpha'}\delta^{\beta\beta'} + \delta^{\alpha\beta'}\delta^{\alpha'\beta}) \quad (\text{S58})$$

where \mathbb{E}_U denotes the Haar average, S is the total spin of the spin coherent state, and J is a constant of proportionality. Via a Taylor expansion of Eq. (S57) with our chosen mean and variance we obtain:

$$\begin{aligned} \mathbb{E}_U [U_t \otimes U_t^\mathcal{T}] &= \mathbb{I} - \frac{Jdt}{2S^2} \sum_{ab} \sum_{\alpha\beta} (-1)^{a+b} (S_a^\alpha S_a^\beta S_b^\alpha S_b^\beta + S_a^\alpha S_a^\beta S_b^\beta S_b^\alpha) + \mathcal{O}(dt^2) \\ &= \mathbb{I} - \frac{Jdt}{2S^2} \left[\sum_a (2S_a^4 - S_a^2) + \sum_{a \neq b} (-1)^{a+b} (2(\mathbf{S}_a \cdot \mathbf{S}_b)^2 + (\mathbf{S}_a \cdot \mathbf{S}_b)) \right] + \mathcal{O}(dt^2) \end{aligned} \quad (\text{S59})$$

where $U^\mathcal{T}$ representing time-reversed, which we convert from U^* , and $a, b \in 0, 1$ are dummy indices corresponding to each replica (i.e. corresponding to either L or R in Fig. S1). The time-reversed unitary is computed through the insertion of the identity $(iY)(iY)^\dagger$, where $iY := \prod_{i=1}^N i\sigma_y$ for all individual spin-1/2 particles indexed by i where N is the total number of spins. Note that this insertion also affects the effective boundary conditions.

We can then reverse the Taylor expansion in Eq. (S59) to get a partition function of the form $\mathbb{E}_U [(U_t \otimes U_t^\mathcal{T})] = \exp(-H_{\text{eff}}^{(1)} dt)$ where $H_{\text{eff}}^{(1)}$ is given by

$$H_{\text{eff}}^{(1)} = \frac{J}{2S^2} \left[\sum_a (2S_a^4 - S_a^2) + \sum_{a \neq b} (-1)^{a+b} (2(\mathbf{S}_a \cdot \mathbf{S}_b)^2 + (\mathbf{S}_a \cdot \mathbf{S}_b)) \right] \quad (\text{S60})$$

For quantities with more than one pair of replicas of U of the form $\bigotimes_{i=1}^k (U_{t,i} \otimes U_{t,i}^\mathcal{T})$ we obtain

$$H_{\text{eff}}^{(k)} = \frac{J}{2S^2} \left[\sum_{ra} (2S_{ra}^4 - S_{ra}^2) + \sum_{ra \neq sb} (-1)^{a+b} (2(\mathbf{S}_{ra} \cdot \mathbf{S}_{sb})^2 + (\mathbf{S}_{ra} \cdot \mathbf{S}_{sb})) \right], \quad (\text{S61})$$

where the indices r, s indicating the pair of replicas under consideration and the indices $a, b \in L, R$ corresponding to the forward and backward time-evolution replicas within each pair.

This Brownian model is equivalent to the random OAT model considered in the main text in the limit of infinitesimal twists. In particular, the random OAT unitary is given by

$$U_{\text{ROAT}} := \prod_t \exp(-iH_{\text{ROAT}} \Delta t), \quad H_{\text{ROAT}} := \chi(\mathbf{S} \cdot \hat{\mathbf{n}})^2, \quad (\text{S62})$$

where \hat{n} is the random axis for a specific one-axis twist, χ is the twisting strength, and Δt instead of dt to indicate non-infinitesimal timesteps. Using the Weingarten calculus [35] to evaluate the mean and variance over all possible rotation axes \hat{n} , we get a mean of 0 and a variance of

$$\begin{aligned} \int_{O(3)} R^{3\alpha} R^{3\beta} R^{3\alpha'} R^{3\beta'} dR &= (\text{Wg}(1^2, 3) + 2\text{Wg}(2, 3)) (\delta^{\alpha\beta} \delta^{\alpha'\beta'} + \delta^{\alpha\beta'} \delta^{\alpha'\beta} + \delta^{\alpha\alpha'} \delta^{\beta\beta'}) \\ &= \frac{1}{15} (\delta^{\alpha\beta} \delta^{\alpha'\beta'} + \delta^{\alpha\beta'} \delta^{\alpha'\beta} + \delta^{\alpha\alpha'} \delta^{\beta\beta'}), \end{aligned} \quad (\text{S63})$$

where $R^{3\alpha}$ is a rotation operator about the z -axis. Note there are four $R^{3\alpha}$ terms present because the second order in the Taylor expansion is quartic in \hat{n} . Performing this disorder average over the random rotations $R^{\alpha\beta}$ we obtain

$$H_{\text{eff,ROAT}}^{(1)} = \frac{\chi^2 S^2 \Delta t}{15J} H_{\text{eff}}^{(1)}. \quad (\text{S64})$$

A similar calculation holds for higher replica moments $k > 1$. Thus, conclusions drawn from analyzing the spectrum of the Brownian model (as done in the following section) apply directly to the random OAT model in the small twisting strength limit.

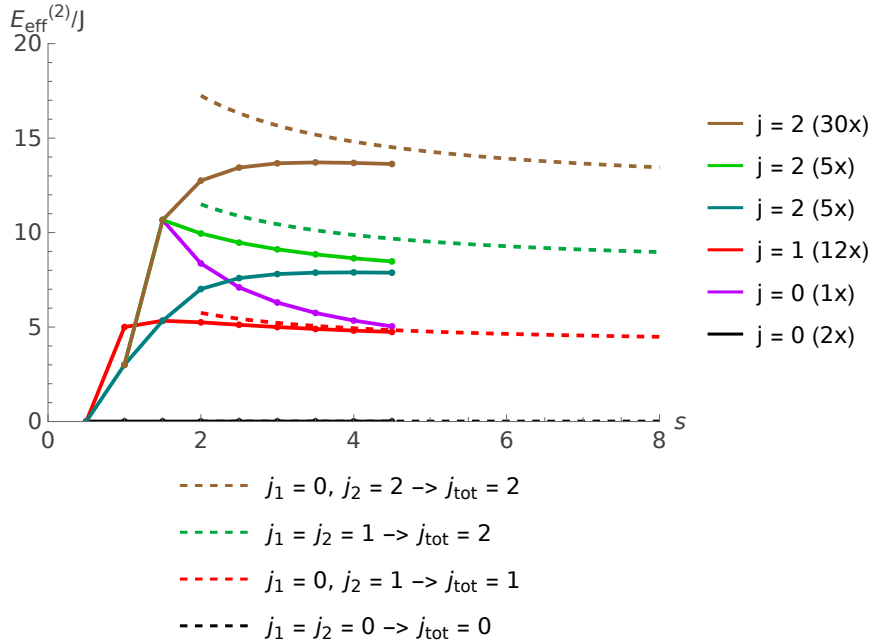


FIG. S8. Effective energy spectrum of $H_{\text{eff}}^{(2)}$ for $k = 2$ for different values of total spin j , where the degeneracies of each level are labelled in the legend – for example, the ground states (black) are doubly degenerate (2x). Analytic results are shown with dashed lines and numeric results are shown with solid lines. Analytics are shown labeled for two different spin pairs, each with independent spin excitations, with both pairs being LR pairs. These also indicate combined angular momentum. The numerics are shown by their total angular momentum only, as specific pairings do not have good quantum numbers associated with them in the non-mean-field case. Therefore, to differentiate, these are also labeled by degeneracy. The analytics and numerics are color-coded to associate different levels together with the sole exception being the excited singlet state in the numerics, which comes from remnants of features lost in the mean-field approximation.

Analysis of Spectra of $H_{\text{eff}}^{(k)}$

In this section we analyze the spectra of the effective Hamiltonians of the Brownian circuit model described in the previous section. The eigenvalue gap of the effective Hamiltonian directly corresponds to the circuit depths needed to generate metrologically useful probe states via these dynamics. We find that the gap is independent of system size, corroborating our numerical evidence that random OAT generates metrologically useful states with a constant number of twists.

The spectrum of the $k = 1$ effective Hamiltonian is exactly solvable yielding energies

$$E_{\text{eff}}^{(1)}(S, j) = \frac{J}{2S^2} j(j+1)(4S(S+1) - j(j+1) - 1) \quad (\text{S65})$$

where j is the total combined spin of both replicas, which can be any integer in the range $0 \leq j \leq 2S$. In the limit that $S \gg j$, $E_{\text{eff}}^{(1)}(S, j) \rightarrow 2Jj(j+1)$, yielding an energy gap of $\Delta E_{\text{eff}}^{(1)} = E_{\text{eff}}^{(1)}(S, j=1) - E_{\text{eff}}^{(1)}(S, j=0) \rightarrow 4J$. Thus, our effective energy gap does not scale with S .

For $k > 1$, we apply mean field theory to Eq. (S61) to obtain the following effective mean-field Hamiltonian for arbitrary k :

$$H_{\text{eff, mf}}^{(k)} = \frac{J}{2S^2} [2k(2S^2(S+1)^2 - S(S+1)) - \sum_{ra < sb} (-1)^{a+b} (4G_{rasb}^2 - (\mathbf{J}_{rasb}^2 - 2S(S+1))(4G_{rasb} + 1))] \quad (\text{S66})$$

where G_{rasb} is the mean-field condition for a given pairing of replica ra to replica sb , and \mathbf{J}_{rasb} is the corresponding combined angular momentum. This mean field effective Hamiltonian is valid for all k , but for the remainder of this section we restrict our attention to $k = 2$.

For $k = 2$, limiting ourselves to just $rLsR$ average singlet pairings—i.e. setting G_{rLsR} to $-S(S+1)$ and other G_{rasb} to 0—we get a spectrum of the following form:

$$E_{\text{eff}}^{(k)} = \frac{J}{2S^2} (4S(S+1) - 1) \sum_{rs} j_{rLsR} (j_{rLsR} + 1) \quad (\text{S67})$$

which, again, yields an effective energy gap of $4J$ in the $S \gg j$ limit, leading us to the conclusion that the approach to randomness for $k = 2$ occurs on constant timescales just like for the $k = 1$ case.

In Fig. S8 we compare our analytical mean-field results at $k = 2$ for the spectrum to numerical results found via exact diagonalization of Eq. (S61). We observe that the low-lying spectrum found via numerics asymptotically approaches the mean field results from the effective Hamiltonian, although we have not fully understood the degeneracies in the spectrum of the finite-size numerics. However, as the eigenvalue gap between ground state and first excited state of the effective Hamiltonian is what we are after, the numerics give us confidence that our approximations are correct and that, indeed, the gap is independent of S .

S6. COMPARISON TO MINIMUM MEAN SQUARE ERROR ESTIMATOR

Here, we compare our butterfly echo protocol with minimum mean square error (MMSE) estimator constructed from a Bayesian perspective. Following Ref. [58], define

$$\Gamma := \int d\theta p(\theta) \mathcal{M}_\theta[\rho]$$

$$\eta := \int d\theta \theta p(\theta) \mathcal{M}_\theta[\rho],$$

where $p(\theta)$ is the prior distribution for the value of the parameter θ . Here, we assume a uniform prior over $\theta \in [0, \theta_{\max}]$. Then, the MMSE estimator for θ is the expectation value of an observable A satisfying

$$\frac{1}{2}\{\Gamma, A\} = \eta. \quad (\text{S68})$$

Assuming $\Gamma > 0$, the solution to this equation is a unique, Hermitian observable given by

$$A = 2 \int_0^\infty d\alpha e^{-\Gamma\alpha} \eta e^{-\Gamma\alpha}. \quad (\text{S69})$$

Assuming a uniform prior we can evaluate, for small θ_{\max} :

$$\begin{aligned} \Gamma &= \frac{1}{\theta_{\max}} \int_0^{\theta_{\max}} d\theta \left[\rho + \frac{\theta^2}{3} \left(\sum_j S_j \rho S_j - \frac{1}{2} \{\rho, S_j^2\} \right) + \mathcal{O}(\theta^3) \right] \\ &= \rho + \frac{\theta_{\max}^2}{9} \left(\sum_j S_j \rho S_j - \frac{1}{2} \{\rho, S_j^2\} \right) + \mathcal{O}(\theta_{\max}^3), \end{aligned} \quad (\text{S70})$$

and

$$\begin{aligned} \eta &= \frac{1}{\theta_{\max}} \int_0^{\theta_{\max}} d\theta \left[\rho\theta + \frac{\theta^3}{3} \left(\sum_j S_j \rho S_j - \frac{1}{2} \{\rho, S_j^2\} \right) + \mathcal{O}(\theta^4) \right] \\ &= \frac{\theta_{\max}}{2} \rho + \mathcal{O}(\theta_{\max}^3), \end{aligned} \quad (\text{S71})$$

where we used Eqs. (S2) and (S3).

To leading order in θ_{\max} , the computation of A is almost trivial. Using the fact that $\rho = \rho^2$ for a pure state, one finds, up to corrections $\mathcal{O}(\theta_{\max}^3)$,

$$A = \theta_{\max} \rho \int_0^\infty d\alpha e^{-2\alpha} = \frac{\theta_{\max} \rho}{2}. \quad (\text{S72})$$

Thus, measuring A for the encoded state $\mathcal{M}_\theta[\rho]$ we obtain the MMSE estimate

$$\begin{aligned} \langle A \rangle &= \frac{\theta_{\max}}{2} \text{Tr}(\rho \mathcal{M}_\theta[\rho]) \\ &= \frac{\theta_{\max}}{2} (1 + \mathcal{D}_\theta[\rho] + \mathcal{O}(\theta^3)). \end{aligned} \quad (\text{S73})$$

Observe the crucial dependence of the uniform prior: even when the true value of the parameter $\theta = 0$ and, thus, $\mathcal{D}_\theta[\rho] = 0$ this estimator returns $\theta_{\max}/2$. Thus, as we expect for a Bayesian estimator taking into account prior information, this estimator is biased.

Up to a normalization factor of $\theta_{\max}/2$ (which biases the MMSE observable), the MMSE observable to first order is to simply compute the overlap of the encoded state $\mathcal{M}_\theta[\rho]$ with the initial state. This is equivalent to the estimator used in the butterfly echo protocol.